Secondary vortex dynamics in the cylinder wake during laminar-to-turbulent transition

Jeffrey McClure,* Colin Pavan, and Serhiy Yarusevych
Department of Mechanical and Mechatronics Engineering, University of Waterloo, Waterloo, Ontario N2L3G1, Canada

(Received 15 October 2018; published 24 December 2019)

Direct numerical simulations of cross-flow over a circular cylinder are performed for Re = 100, 220, 300, 800, and 1575, spanning laminar-to-turbulent transition and progressively capturing the initial two-dimensional global instability, three-dimensional mode A^* and mode B instabilities, a distinct $B+$ instability, and Kelvin-Helmholtz instability, respectively. For Re $\geqslant$ 800, vortex topology and snapshot proper orthogonal decomposition (sPOD) analyses of the three-dimensional flow fields reveal significant alterations in the dynamics of secondary vortices preceding shear layer transition, denoted $B+$ instability. The defining instantaneous characteristic of $B+$ instability is hairpin vortex formations straddling mode B structures. An iterative scheme for three-dimensional vortex tracking is employed and the probability density functions of secondary vortex statistics show a marked broadening for Re $\geqslant$ 800, associated with the increased variability in the wake vortex dynamics. The significant broadening of the modal energy spectrum of the sPOD serves as a marker for the topological change to $B+$ instability, reflecting the increased complexity of the dynamics. Integral effects on the primary shedding instability due to the increase in secondary vortex formation are deduced through a decomposition of the vorticity transport in the wake. An increase in streamwise and transverse reorientation of spanwise vorticity is identified for increasing Re, leading to a decrease of up to 20% in the advected spanwise vorticity of the primary vortices. Therefore, the reorientation of spanwise vorticity may be identified as a subsidiary mechanism for the attenuation of fluctuating structural loads in the basic cylinder wake.

DOI: 10.1103/PhysRevFluids.4.124702

I. INTRODUCTION

Flow past a circular cylinder is fundamental to the study of bluff body aerodynamics. Features of the incompressible wake development are dependant exclusively on Reynolds number (Re) for an infinite, smooth cylinder in undisturbed cross-flow, and von Kármán vortex shedding is present over a wide range of Re encompassing various practical applications [1]. The unsteady wake vortex dynamics influence the mean and fluctuating structural loads on the cylinder. Critically, wake-induced pressure and velocity fluctuations at the cylinder surface may lead to the emergence of significant structural vibrations [2–4] and acoustic noise [5]. The cylinder wake is receptive to both passive [4,6,7] and active control methods [8–10], motivating the need for a detailed quantitative understanding of the wake structure through laminar and turbulent flow regimes.

A brief overview of unsteady aspects of cylinder wake development can be obtained by considering the changes in wake dynamics with Re. For Re $\gtrsim$ 50 [1], a global instability leads to periodic, alternate shedding of two-dimensional wake vortices near a constant frequency (f_S). The periodic

*jejmcclu@uwaterloo.ca

wake becomes three-dimensionally unstable for $\mathrm{Re} \gtrsim 190$ [11] with initiation of the mode A elliptic instability in the primary vortex cores. The mode A instability induces the formation of vortex loops between subsequently shed spanwise vortices at a spanwise wavelength of $\lambda_z/D \approx 3$–4 [12,13]. The mode A structures remain stable for only a relatively small number of shedding cycles after inception, before large scale vortex dislocations develop [14–16] and the wake state is termed mode A^*. For $220 \lesssim \mathrm{Re} \lesssim 270$, the mode B hyperbolic instability develops in the saddle point region between the primary rollers and is characterized by smaller scale streamwise vortex pairs of spanwise wavelength $\lambda_z/D \approx 1$ [12,17,18]. The wake topology intermittently switches between mode A^* and B in this Re range, with the probability of the mode B state increasing at higher Re [18]. For $\mathrm{Re} > 300$, secondary wake vortices form randomly and appear at smaller spatial scales [19–21]. The emergence of chaotic dynamics in this Re range has been attributed to period-doubling associated with subharmonic growth of the mode A instability [19,22], period-doubling related to the formation of hairpin vortex structures every other shedding period [21], or a Ruelle-Takens-Newhouse route to chaos due to competition of $\geqslant 3$ permissible unstable mode A wavelengths within the domain [23]. For $1.0 \times 10^3 \lesssim \mathrm{Re} \lesssim 2.0 \times 10^5$, the convective Kelvin-Helmholtz (KH) instability in the separated shear layer leads to KH-vortex roll-up at a distinct frequency (f_{KH}), before the formation of wake vortices [24]. The wavelength of the KH-vortices varies significantly with Re, and the ratio f_{KH}/f_S increases proportional to $\mathrm{Re}^{0.67}$ [25]. Following formation, the KH-vortices deform substantially [26], amalgamating into the von Kármán rollers, or tilting and straining rapidly in regions between them [27].

The quantitative description of the secondary vortex dynamics associated with the three-dimensional instabilities for $\mathrm{Re} \gtrsim 190$ has largely been limited to planar statistics from experimental and numerical data. With increasing Re, the maximum streamwise vorticity in the wake increases and eventually exceeds the peak spanwise vorticity due to rapid stretching of streamwise vortices in the high strain region between the primary vortices [17,27–31]. As structures advect downstream following formation, maximum vorticity decays due to vorticity diffusion and cross-annihilation, with the decay rate increasing with Re [29]. Similarly, the circulation of the spanwise vortices attained at formation, varying within $0.8 < \Gamma_z/\pi U_o D < 1.2$ depending on Re [29,32,33], decays with streamwise distance [29] due to the entrainment of opposite sign vorticity bearing fluid across the wake centerline. The streamwise circulation of the mode A vortices ($\Gamma_x/\pi U_o D = 0.3$) is greater than the mode B vortices ($\Gamma_x/\pi U_o D = 0.16$); however, the streamwise circulation of mode B vortices increases with Re for $160 \geqslant \mathrm{Re} \geqslant 500$ [31]. For $\mathrm{Re} = 2 \times 10^3$ and $\mathrm{Re} = 1 \times 10^4$, measurements of the transverse circulation of the secondary structures yield smaller estimates ($\Gamma_y/\pi U_o D = 0.095 - 0.14$) compared to the streamwise circulation ($\Gamma_x/\pi U_o D = 0.2 - 0.26$) [28,29], and a statistical analysis of centroid positions indicates a most likely vortex inclination of 43–48° from the horizontal. A number of studies indicate a relationship between the circulation of the primary and secondary vortices, attributing a decrease in spanwise vortex circulation to enhanced turbulent entrainment of opposing vorticity across the wake [32,34] or direct transfer from spanwise oriented vorticity to the secondary vortices [35].

The dynamics of the flow can be elucidated using the proper orthogonal decomposition (POD), which expresses the fluctuating velocity field in an energy optimal spatial basis on which the primary dynamics lie on an attractor described by the most energetic modes [36]. For the cylinder wake, the two most energetic POD modes along with corresponding temporal coefficients form a pair that captures the main dynamics of von Kármán vortex shedding across a wide range of Re in the subcritical regime [7,34,37–41]. The third most energetic mode is often a solitary mode containing lower frequency modulations of the base flow, and is termed the shift mode [42,43]. Higher-order modes include higher harmonics of the first mode pair, occurring in pairs resembling the structure of the global instability modes [44].

Floquet and global stability analyses have been successful in predicting the most unstable wavelengths and critical Re to excite global shedding, mode A, and mode B instabilities [1,11]. However, a quantitative description of the secondary vortex developments and their integral effects

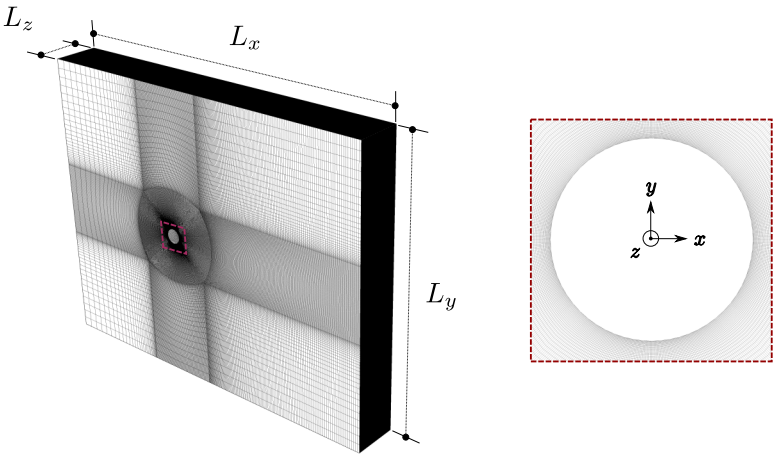

FIG. 1. Hybrid structured O-type and H-type computational grid for Re = 1575. L_x, L_y, L_z denote the streamwise, transverse, and spanwise domain extents, respectively.

on the primary von Kármán vortices, which are primarily responsible for fluctuating wake pressures and structural loads, remains unclear. In particular, a comprehensive description of the secondary vortex dynamics beyond mode B (Re > 300) accompanying turbulent transition of the wake merits a more detailed investigation [23]. Measurements of the quantitative properties of primary and secondary vortices encounter limitations associated with planar analysis and/or finite spatial resolution [45]. Therefore, in the current study, high resolution, three-dimensional direct numerical simulations (DNS) are performed and detailed measures of secondary vortex statistics are obtained and analyzed through the application of a novel iterative, three-dimensional vortex identification scheme.

II. NUMERICAL METHODOLOGY

A. Direct numerical simulations

Numerical solutions to the three-dimensional, incompressible Navier-Stokes equations are computed for uniform cross-flow over a circular cylinder for Re = 100, 220, 300, 800, and 1575. The equations are solved directly using the finite volume code ANSYS CFX 14.0. A second-order, blended spatial discretization scheme and a second-order, implicit, backward Euler time marching scheme are employed with pressure-velocity coupling handled by Rhie-Chow interpolation. The computational domain and grid for the Re = 1575 solution is depicted in Fig. 1. The grid topology is structured with an O-type block surrounding the cylinder and an H-type block in the remaining regions, which is a hybrid mesh configuration commonly used in simulations of bluff body flows [6,46,47]. The boundary conditions are prescribed as follows: uniform velocity ($u = [U_o, 0, 0]$) at the inlet, zero average static pressure condition at the outlet, no-slip condition ($u = [0, 0, 0]$) at the cylinder surface, and a free-slip condition ($u_n = 0$, $\partial u_t/\partial n = 0$) at the remaining domain boundaries. The coordinate system used for data presentation has the origin located at the mid-span of the cylinder (Fig. 1) and the x, y, and z directions denote the streamwise, transverse, and spanwise directions, respectively.

To accommodate the length and time scale changes with Re, the computational grid and domain are adapted appropriately (Table I). Simulations are performed on a two-dimensional grid for Re = 100, and three-dimensional grids for Re = 220–1575. For Re = 800 and 1575, the grid densities (Table I) are selected based on the sizing recommendations of Moin and Manesh (1998) [48], which specify that the smallest resolved length scale is on the order of the Kolomogorov scale [$O(\eta)$], such

TABLE I. Computational domain and grid parameters for each Re.

Re_D	Nodes	$R\Delta\theta/\eta \times \Delta r/\eta \times \Delta z/\eta$	$\Delta t/\tau$	L_x/D	L_y/D	L_z/D
100	1.2×10^5	$0.53 \times 0.08 \times 0$	0.12	24	35	0
220	5.0×10^6	$0.89 \times 0.49 \times 3.60$	0.18	24	35	18
300	1.7×10^6	$1.21 \times 0.66 \times 4.88$	0.19	24	35	6
800	1.1×10^7	$1.20 \times 0.69 \times 3.82$	0.21	24	35	6
1575	2.9×10^7	$1.59 \times 0.71 \times 2.85$	0.17	24	35	3.14

that the majority of energy containing eddies are resolved. The grid density employed in the current study compares well with previous studies employing second-order, finite volume DNS codes at comparable Re [16,49,50]. Specifically, Wissink and Rodi (2008) [49] achieve grid convergence for a circular cylinder in cross-flow at Re = 3300 for a mesh with near wall spacing $R\Delta\theta/\eta = 1.27$, $\Delta r/\eta = 0.48$, and $\Delta z/\eta = 3.87$, where $R\Delta\theta$, Δr, and Δz are linear circumferential, radial, and spanwise spacings, respectively. These values compare well with the final grid parameters listed in Table I for each Re, when the estimate $\eta = D(1/\mathrm{Re})^{0.75}$ is used for the Kolmogorov length scale. Based on the results of previous numerical studies, a spanwise domain extent of $L_z/D = 6$ is chosen for Re = 300 and 800, an extent of $L_z/D = 18$ is chosen for Re = 220 to accommodate the larger wavelength mode A instability [51], and an extent of $L_z/D = 3.14$ is chosen for Re = 1575 [49]. Solutions are stepped forward in time at a temporal resolution (Table I) that ensured a maximum Courant number ($u\Delta t/\Delta x$) of less than one. Solution variables are sampled when a streamwise velocity signal at $x/D = 5$, $y/D = 0.75$, and $z/D = 0$ reached a quasisteady state, and data are collected for a minimum of 16 vortex shedding cycles. Figure 2 presents transverse wake profiles of mean velocity and normal Reynolds stress statistics for Re = 1575. The sectional fluctuating lift and drag coefficients are calculated from the total forcing on the cylinder, adjusted to account for the spanwise correlation of the fluctuating lift [$R_{LL}(s)$] or drag [$R_{DD}(s)$] [52]. The shedding frequency (f_s) is estimated by a spectral analysis of the streamwise wake velocity fluctuations sampled at $x/D = 5$ and $y/D = 0.75$, with a resolution of $\pm 0.0020 - 0.0096 f D/U_o$, depending on Re. A detailed grid independence study was performed for Re = 100 and 300, ensuring further increases in the domain extents (L_x, L_y, L_z) and grid density ($R\Delta\theta$, Δr, Δz) resulted in changes in f_S and C_D of less than 1% and C_L' less than 3%. Moreover, Secs. III A 1 and III A 2 include comparisons of the results against collated experimental data and characterize their correspondence.

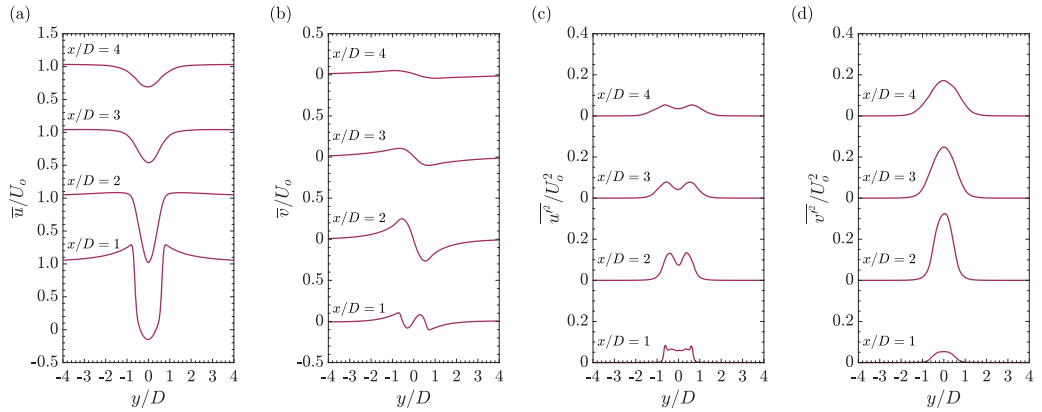

FIG. 2. Transverse profiles of wake statistics for Re = 1575: (a) mean streamwise velocity, (b) mean transverse velocity, (c) normal streamwise Reynolds stress, (d) normal transverse Reynolds stress.

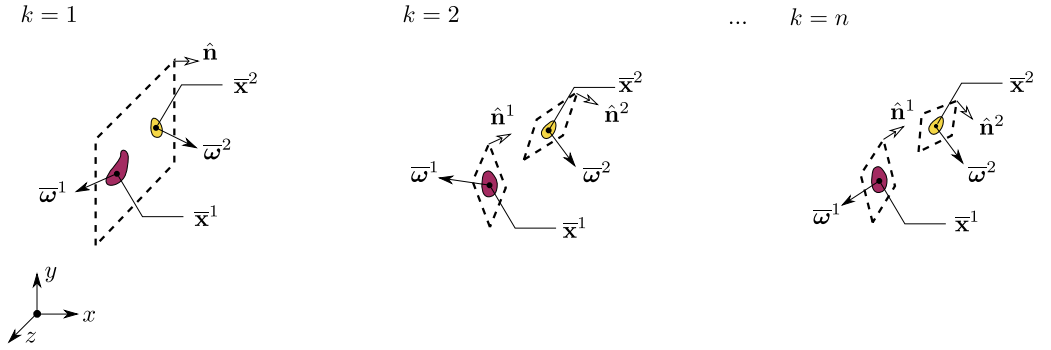

FIG. 3. Schematic of the iterative, three-dimensional vortex detection code. The code converges on the individual vortex orientation ($\overline{\boldsymbol{\omega}}^j$), centroid ($\overline{\mathbf{x}}^j$), diameter ($d^j$), and circulation ($\Gamma^j$).

B. Three-dimensional vortex tracking algorithm

The quantitative analysis of vortex statistics in three dimensions is challenging due to the need to resolve the bounds of the vortices along with their orientation and position in three-dimensional space. Although high fidelity three-dimensional vortex tracking algorithms have been introduced [53], no established tool exists for establishing vortex orientation; hence, to facilitate the accurate measurement of statistics pertaining to the primary and secondary vortices, an iterative, three-dimensional, vortex identification code is developed. The code operates as follows: for a three-dimensional realization of a velocity field at a certain time, $\mathbf{u}(\mathbf{x}, t)$, an initial streamwise normal plane is specified at $x/D = 2.5$ and vortices intersecting the plane are detected, where the j^{th} vortex is defined by its boundary, Ω^j. The code then computes the three-dimensional orientation ($\bar{\boldsymbol{\omega}}^j$), centroid ($\bar{\mathbf{x}}^j$), diameter ($d^j$), and circulation ($\Gamma^j$) for the j vortices intersecting the plane, as defined in Eqs. (1)–(4):

$$\bar{\boldsymbol{\omega}} = \frac{\int_\Omega \boldsymbol{\omega} dA}{\| \int_\Omega \boldsymbol{\omega} dA \|}, \tag{1}$$

$$\bar{\mathbf{x}} = \frac{\int_\Omega \mathbf{x}(\boldsymbol{\omega} \cdot \hat{\mathbf{n}}) dA}{\int_\Omega (\boldsymbol{\omega} \cdot \hat{\mathbf{n}}) dA}, \tag{2}$$

$$d = \sqrt{\frac{4}{\pi} \int_\Omega dA}, \tag{3}$$

$$\Gamma = \int_\Omega (\boldsymbol{\omega} \cdot \hat{\mathbf{n}}) dA. \tag{4}$$

The code operates by detecting vortices according to the schematic shown in Fig. 3. In the first iteration ($k = 1$), a binary image is obtained by thresholding the input slice plane for $Q > 0.01$, and continuous regions of the thresholded criterion are identified (e.g., yellow and purple regions of high streamwise vorticity in Fig. 3). The regions which intersect the domain boundaries are discarded, thereby avoiding calculating statistics based on partially resolved vortices. Each identified region defines an independent vortex Ω^j and the first iteration estimate for the vortex orientation [Eq. (1)] and centroid [Eq. (2)] are calculated. In general, the vortex orientation will not be aligned with the original sample plane, rendering any statistics calculated inaccurate [29]; hence, in the second iteration ($k = 2$), each vortex region is resampled from a plane normal to the average of the previous iteration vortex orientation and slice plane normal vector ($\hat{\mathbf{n}}^{(k+1)} = \hat{\mathbf{n}}^{(k)}/2 + \overline{\omega}^{(k)}/2$), which intersects the previous iteration vortex centroid ($\overline{\mathbf{x}}^{(k)}$). From the resampled planes, continuous regions of the thresholded criterion field are once again detected and the one whose centroid is closest to that of the previous iteration is identified. The vortex orientation and centroid position are

TABLE II. Sampling parameters and domain extents utilized for the sPOD.

Re_D	S_x/D	S_y/D	S_z/D	$\Delta x/D$	N	f_{acq}/f_S
100	[0.5,8.5]	[−4, 4]	–	0.05	1300	25.5
220	[0.5,8.5]	[−4, 4]	[−3, 3]	0.05	900	18.2
300	[0.5,8.5]	[−4, 4]	[−3, 3]	0.05	1000	18.4
800	[0.5,8.5]	[−4, 4]	[−3, 3]	0.05	600	25.8
1575	[0.5,8.5]	[−4, 4]	[−1.5, 1.5]	0.05	700	46.1

then updated based on Eqs. (1) and (2). Since the updated centroid may now lay off the original input plane, the average between the previous iteration centroid and the centroid calculated on the new sample plane is projected onto the original slice plane to carry forward instead. The vortex detection code is considered converged when the centroid location residual ($\overline{\mathbf{x}}^{(k+1)} - \overline{\mathbf{x}}^{(k)}$) becomes less than the grid resolution, Δx. Once converged, the vortex boundaries are recomputed using a range of vorticity thresholds, $\alpha = \{0.01, 0.025, 0.05, 0.1, 0.25\}$, defining contours of constant vorticity $\alpha\|\omega\|_{\max}$, and circulation is then measured by a linear extrapolation of the data at the computed thresholds to $\alpha = 0$. This final step mitigates erroneous estimates of circulation inherent to a subjective selection of a given contour threshold, as well as under predictions of vortex circulation when boundaries are defined based on a given continuous Q-criterion contour.

C. Snapshot proper orthogonal decomposition

The fluctuating velocity fields $[\mathbf{u}'(\mathbf{x}, t)]$ are decomposed using the snapshot proper orthogonal decomposition (sPOD), a data-based, energy optimal modal decomposition which provides a method for deducing the dynamics of coherent structures in turbulent flows [36,54]. The decomposition involves solving the eigenvalue problem in Eq. (5), where the dot product on the left-hand side defines the two-time velocity correlation matrix:

$$[\mathbf{u}'(\mathbf{x}, t_i), \mathbf{u}'(\mathbf{x}, t_j)]\boldsymbol{\psi}_i(\mathbf{x}) = \lambda_j \boldsymbol{\psi}_j(\mathbf{x}), \tag{5}$$

$$\boldsymbol{\phi}_n(\mathbf{x}) = \mathbf{u}'(\mathbf{x}, t)\boldsymbol{\psi}_n(\mathbf{x})\frac{1}{\sqrt{\lambda_n}}. \tag{6}$$

The decomposition separates the field into spatial modes $\boldsymbol{\phi}_n(\mathbf{x})$ and time dependent temporal coefficients $a_n(t)$ [Eqs. (7) and (8)]. The spatial modes and the temporal coefficients form distinct orthogonal sets, and the modal energy (λ_n) may be determined by the autocorrelation of the corresponding temporal coefficient [Eq. (9)]:

$$\mathbf{u}(\mathbf{x}, t) = \bar{\mathbf{u}}(\mathbf{x}) + \sum_{n=1}^{N} a_n(t)\boldsymbol{\phi}_n(\mathbf{x}), \tag{7}$$

$$a_n(t) = [\mathbf{u}(\mathbf{x}, t), \boldsymbol{\phi}_n(\mathbf{x})], \tag{8}$$

$$\lambda_n = \overline{a_n(t)^2}. \tag{9}$$

The sPOD was performed on a uniformly sampled ($\Delta x/D = 0.05$) subset of the DNS solution to make the problem computationally tractable. The domain was restricted to the wake of the cylinder ($0.5 \geqslant S_x/D \geqslant 8.5$, $-4 \geqslant S_y/D \geqslant 4$), with the spanwise extent and number of snapshots dependent on Re (Table II).

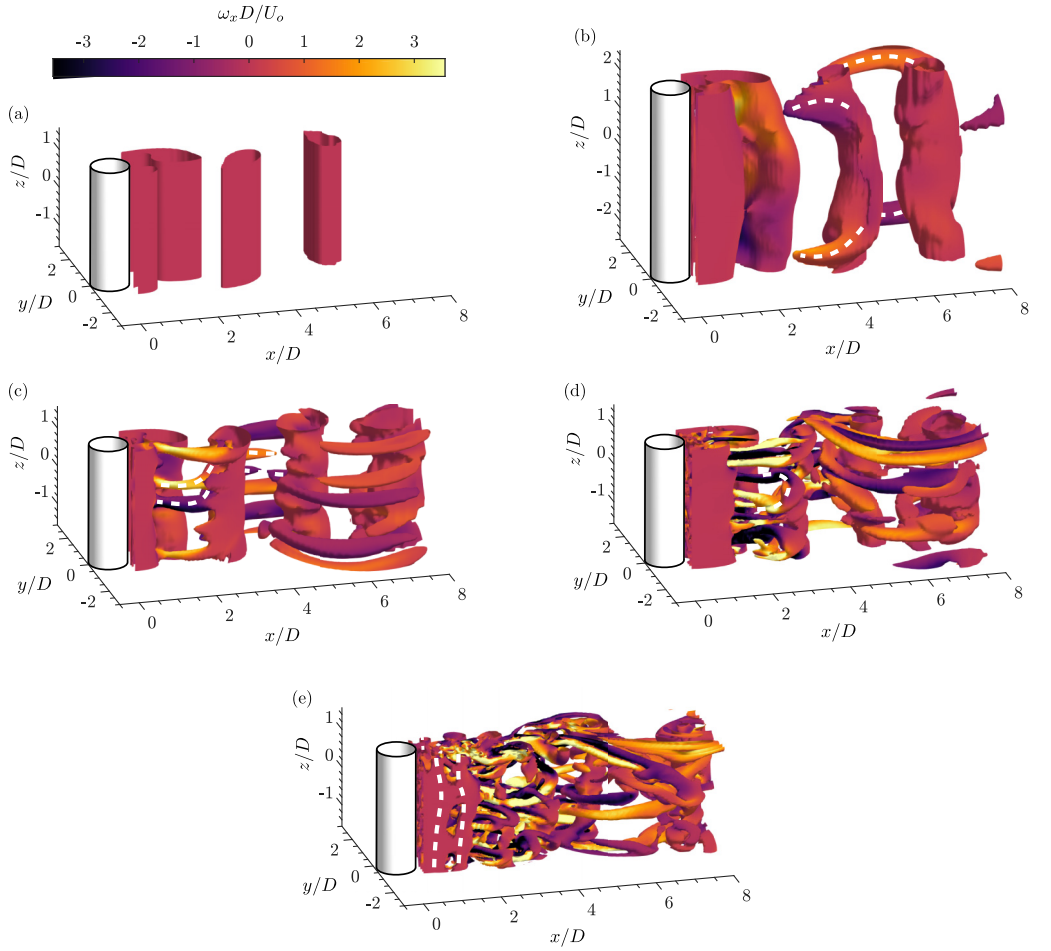

FIG. 4. Vortex shedding topological regimes for (a) Re = 100, (b) Re = 220, (c) Re = 300, (d) Re = 800, and (e) Re = 1575. Vortices are visualized using the Q-criterion ($Q = 0.01$) [55], colored by the streamwise vorticity.

III. RESULTS

A. Overview of primary flow quantities

1. Vortex dynamics

Figure 4 presents isosurfaces of $Q = 0.01$ [55]. Positive values of Q correspond to flow regions where vorticity dominates over shear and, hence, the isosurfaces serve as a vortex identification criterion. The isosurfaces are colored by streamwise vorticity to show the orientation of the secondary vortices. Defining vortex structures for each Re are further highlighted by white dashed lines to aid the discussion. For Re = 100 [Fig. 4(a)], the two-dimensional simulation captures the parallel shedding mode in the laminar shedding regime [56], where elliptically shaped vortices are shed alternately into the wake. For Re = 220 [Fig. 4(b)], the mode A instability [12] of the primary spanwise vortices is amplified, beginning as an elliptic instability in the cores of the spanwise vortices before further amplification in the high strain region of hyperbolic flow connecting the primary rollers [13]. After the initial instability growth, large-scale vortex dislocations develop, resulting in the mode A^* regime, typical of both DNS [18] and experiments [20]. For Re = 300

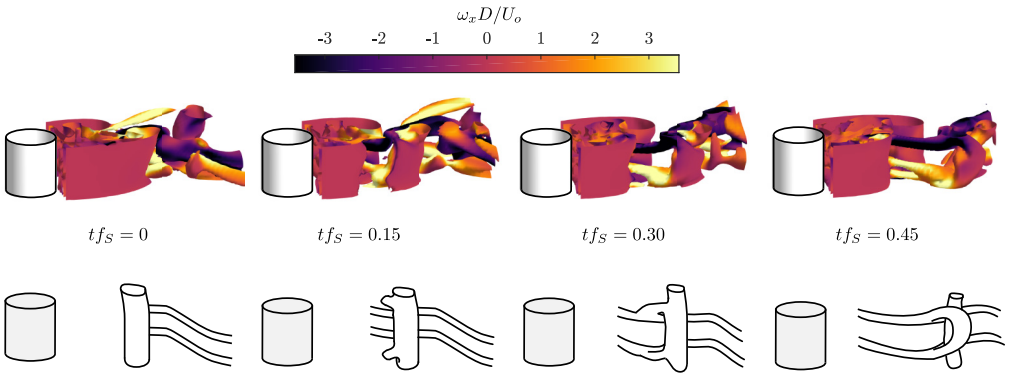

FIG. 5. Time sequence of a hairpin vortex formation for Re = 800. Vortices are visualized using the Q-criterion ($Q = 0.01$), colored by the streamwise vorticity.

[Fig. 4(c)], the mode B instability is amplified, which has been linked to a hyperbolic instability of the highly strained vorticity layer between the vortex cores [12]. The mode B instability form predominantly in pairs of streamwise vortices of opposing sign, such as those highlighted in Fig. 4(c), and can be observed persisting for Re = 800 [Fig. 4(d)] and 1575 [Fig. 4(e)]. Besides exhibiting different characteristic wavelengths, the mode A and mode B vortices have topological differences. At a given spanwise location, the mode A instability switches orientation between each subsequently shed vortex [see the highlighted vortices at $z/D \approx 1.5$, Fig. 4(b)]. However, the mode B instability induces the formation of similar structures with the same orientation between subsequently shed vortices, leading to a continuous weaving of vortex filaments through the vorticity sheets between the main spanwise rollers [see the highlighted vortices at $z/D \approx 0$, Fig. 4(c)]. For Re = 800 [Fig. 4(d)] and Re = 1575 [Fig. 4(e)], the mode B structures remain to be the dominant secondary structures in the wake, but additional secondary structures of varying scales and orientation also begin to form and produce more complex vortex interactions in the wake.

A comprehensive description of the vortex dynamics beyond Re > 300 has yet to be established [20,21,23], although the various stages of KH roller development in the separated shear layers [Fig. 4(e)] [24] for Re $\gtrsim$ 1000 has been considered in a number of studies [27,57–59]. A qualitative description of the evolution of secondary structures and the resulting changes in the wake vortex dynamics can be obtained from the Q isosurfaces in Figs. 4(d) and 4(e). Specifically, mode B vortices are identified for Re = 800 as strong streamwise structures which weave and connect between the primary vortices. Additional structures are identified pinching off from the spanwise vortex furthest from the wake centreline, forming hairpin vortices which straddle the dominant mode B structures [see the highlighted vortex in Fig. 4(d)]. For Re = 1575, the KH instability leads to convective amplification of perturbations in the shear layer and shedding of KH vortices prior to the formation of the main spanwise rollers, with the KH vortices following deformation patterns of the stronger structures in the wake or being amalgamated into them [highlighted vortices at $x/D \approx 0.6$ and 1, Fig. 4(e)] [27]. The hairpin deformations have been previously identified by Mittal and Balachandar [21] for Re = 525 as repeating every other shedding cycle, which is an observation repeated in the current results and is a mechanism consistent with the period doubling hypothesis of cylinder wake transition proposed in Karniadakis and Triantafyllou [19]. Hence, a defining characteristic of instability following the $2D \rightarrow A \rightarrow A^* \rightarrow B$ transition sequence of the cylinder wake with increasing Re is that of hairpin-like structures which straddle the mode B instability. The formation of a prototypical hairpin structure is shown in the time sequence presented in Fig. 5 for Re = 800, and shows the process of pinching off vorticity from the main spanwise roller, which then reorients and merges with the mode B vortices to form the legs of a hairpin. The wake state following the excitation of this instability is denoted $B+$, hereafter. The results for

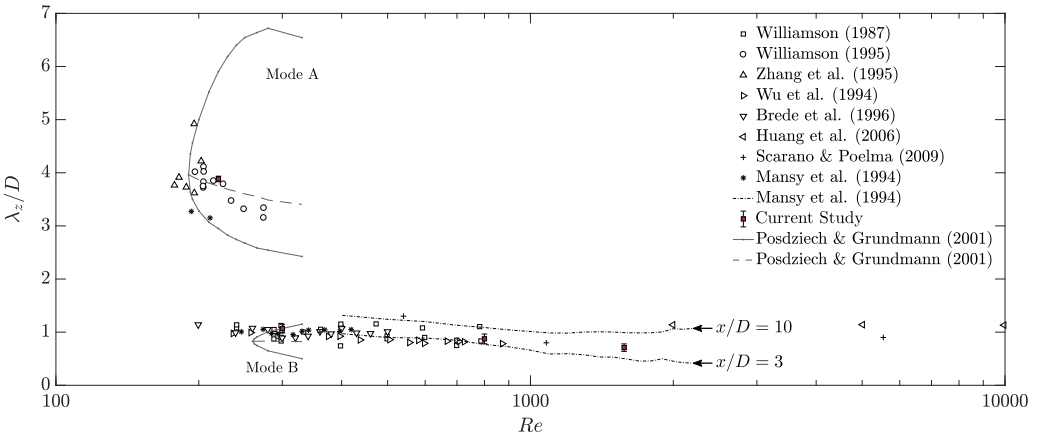

FIG. 6. Dominant spanwise wavelength of the secondary structures in the cylinder wake overlayed on three-dimensional Floquet stability analysis results [60]. Solid dotted lines indicate the neutral curve and dashed lines indicate the most unstable wavelengths.

Re = 300 [Fig. 4(c)] show preliminary deformation of the upper layer of the spanwise vortices induced by the precense of the mode B instability structures. This indicates that inception of the instability is linked to the presence of the mode B structures, explaining its absence as a distinct mode in previous Floquet instability analysis, which considers phase averaged fields with respect to the primary instability that would not contain mode B structures [60].

Figure 6 shows the dominant spanwise wavelengths (λ_z) of the secondary vortex structures in the wake, where the current data are shown amongst the collated results of experimental, numerical, and instability analyses [17,20,29–31,60–62]. The mean wavelengths were estimated using the two-dimensional correlation of the streamwise vorticity in the y-z plane at $x/D = 2.5$ [Eq. (10)] and computing the spanwise distance between adjacent dominant peaks:

$$R_{\omega_x}(x_o, y, y', z, z') = \frac{\overline{\omega_x(x_o, y, z)\omega_x(x_o, y', z')}}{\sigma_{\omega_x}\sigma_{\omega_x'}}. \tag{10}$$

In general, the spanwise wavelengths are observed to increase with streamwise distance [62]; thus, the measurement plane at $x/D = 2.5$ was selected as it is located immediately downstream from the formation of the primary and secondary vortices in all cases. For Re = 220, the autocorrelation analysis was performed using only data during the initial growth period of the mode A instability, to compare with previously published results [20]. The results for each Re (Fig. 6) compare favorably to the results of previous experimental studies and instability analyses [11,60]. Notably, Fig. 6 shows a wide band of unstable wavelengths present for the mode A instability at Re = 220 [Fig. 4(b)], which results in the observed vortex dislocations [15] due to differences in the wavelengths of excited modes [13]. Henderson [23] argues that the competing mode A wavelengths lead to a wake with chaotic dynamics. However, it is unclear in the current results whether the complexity observed for Re = 220 [63] is truly chaotic or simply due to complex interactions occurring between the excited modes. For Re $\geqslant$ 300, the mode B vortices remain the dominant streamwise structures in the wake, however, their spanwise wavelength progressively decreases with increasing Re.

2. Structural loads

Figures 7(a)–7(c) plot the RMS fluctuating lift coefficient (C_L'), mean drag coefficient ($\overline{C_D}$), and sectional RMS drag coefficient (C_D'), respectively, comparing the DNS data to a compilation of both experimental and numerical literature sources [6,9,16,23,34,50,64–86]. In each case, the total RMS coefficients are converted to sectional RMS coefficients by evaluating the spanwise correlation of

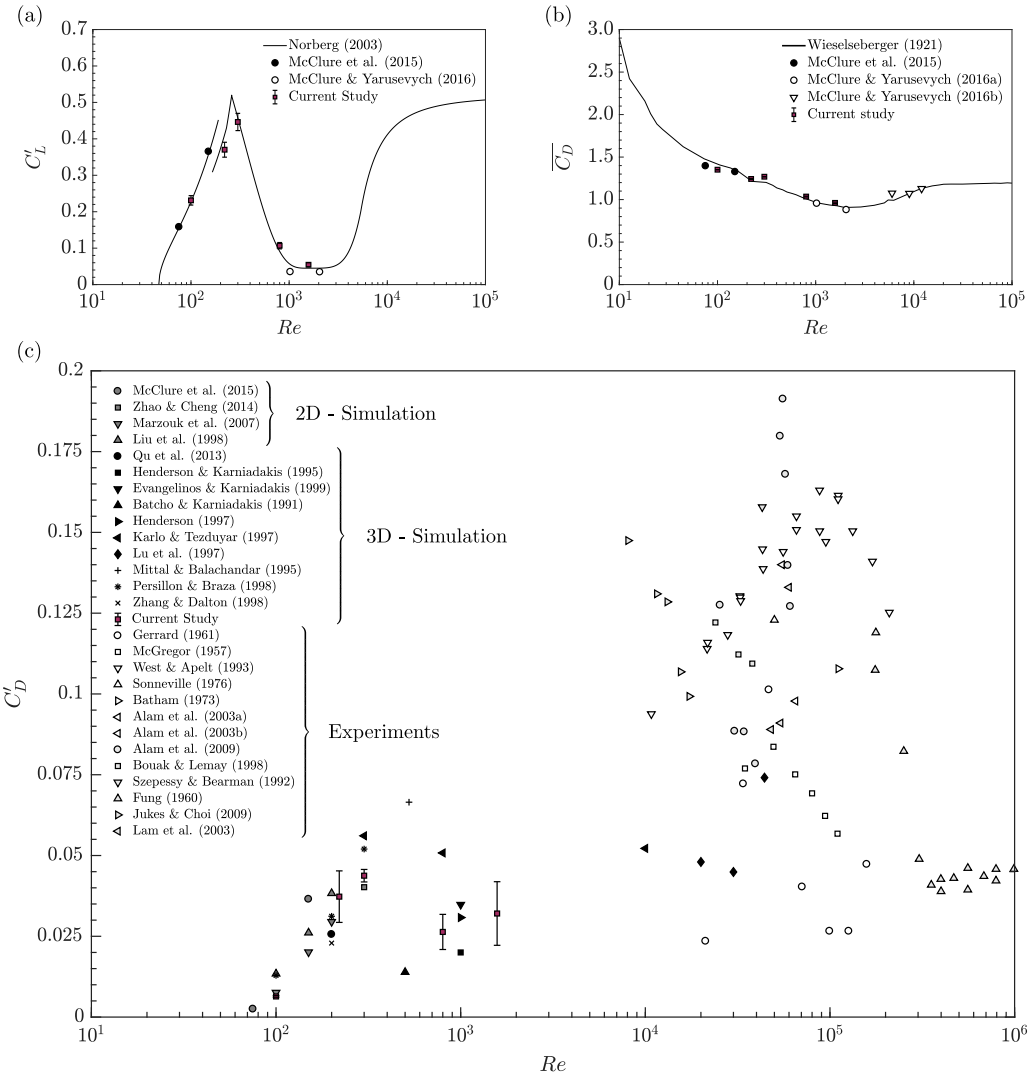

FIG. 7. (a) Sectional RMS lift coefficient, (b) mean drag coefficient, and (c) sectional RMS drag coefficient versus Re.

the fluctuating pressure lift $[R_{LL}(s)]$ and fluctuating pressure drag $[R_{DD}(s)]$ across the model length $0 \leqslant s \leqslant L_z$ for the duration of the integrated time period used for statistics. The sectional RMS force coefficients are then computed from the relations in Eqs. (11) and (12) [52]:

$$\frac{C'_{L,T}}{C'_L} = \frac{1}{L_z}\left[2\int_0^{L_z}(L_z - s)R_{LL}(s)ds\right]^{1/2}, \tag{11}$$

$$\frac{C'_{D,T}}{C'_D} = \frac{1}{L_z}\left[2\int_0^{L_z}(L_z - s)R_{DD}(s)ds\right]^{1/2}. \tag{12}$$

The current results compare favorably with the data from previous studies up to the quantified uncertainty bounds, which accounted for statistically dependent sampling of the data [87] using an effective number of samples $N_{\text{eff}} = N\Delta t/2T_{\text{int}}$, where T_{int} is the integral time scale measured

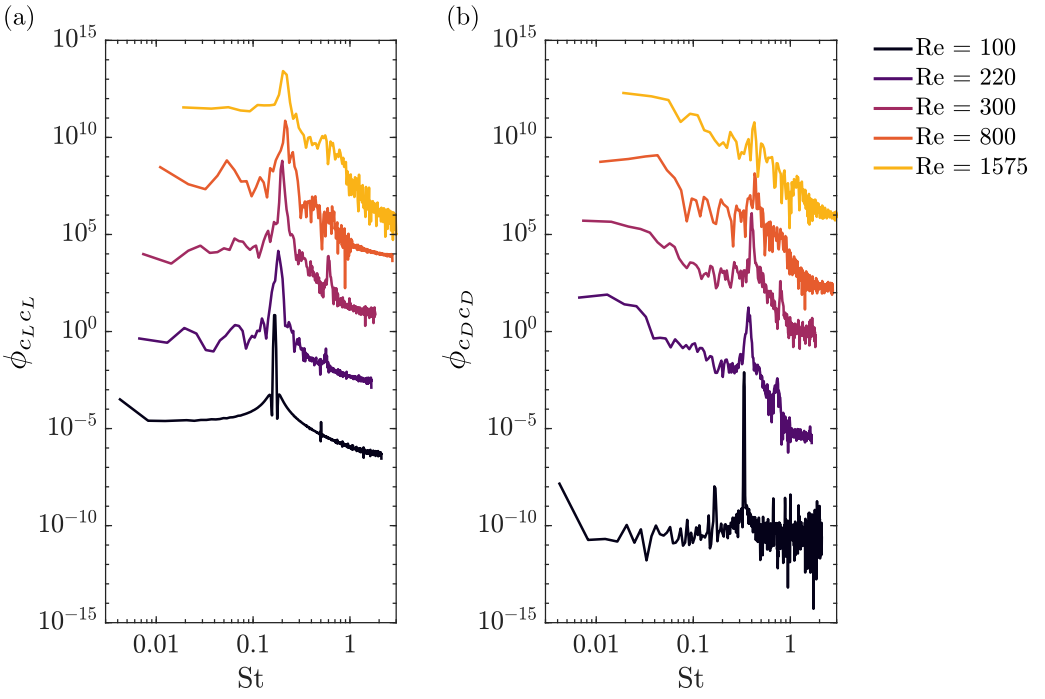

FIG. 8. Power spectral density of the (a) lift force fluctuations and (b) drag force fluctuations for each Re. Spectral resolution varies from 0.004–0.019fD/U_o for Re = 100 to Re =1575. Spectra are offset vertically by factors of 10^4 as Re increases.

by the zero crossing of the signal autocorrelation function. Notably, uncertainty in the fluctuating quantities in Figs. 7(a) and 7(c) is higher for cases dominated by low-frequency fluctuations in the forces, leading to an increase in the integral time scale. The data for the sectional RMS lift coefficient [Fig. 7(a)] resolve a substantial minimum in C_L' for approximately 800 < Re < 5000, where only the 3D simulations of Norberg [88] and experiments of McClure and Yarusevych [34] are available for comparison. The experimental measurements produce marginally lower C_L' compared to the simulations, which may be attributed to uncorrelated end cells present in the experiment, causing a violation of the spanwise homogeneity assumption invoked in the derivation of Eq. (11). The mean drag coefficient results [Fig. 7(b)] compare well with the drag curve of Wieselsberger [64] over the Re range investigated. Minor discrepancies from the trend are in agreement with deviations at comparable Re seen in other recent investigations [16,89]. Measurements of C_D' [Fig. 7(c)] show a high degree of scatter across multiple studies. This perhaps is partially responsible for the fact that C_D' data are more scarcely documented in the literature, even though the forcing is nonnegligible and is in fact comparable in magnitude to C_L' for Re $\approx 10^3$, which can have important implications for vortex-induced vibration (VIV) [90–92]. The interpretation of Fig. 7(c) requires the knowledge that C_D' can have significant energy concentrated in both a narrow frequency band around twice the shedding frequency $2f_S$ [77], and a wider band at low frequencies. The component at $2f_S$ is caused by the formation of two low pressure vortex cores just downstream of the cylinder every shedding period, hence its magnitude is dependent on the formation length (l_f) and follows trends in C_L' closely [Fig. 7(a)]. The low-frequency components are associated with a slow modulation of the base flow [86], leading to drifting of the base pressure on the aft of the cylinder surface. Spectral analysis of the drag force fluctuations presented in Fig. 8 indicates that the amplitude of drag fluctuations at $2f_S$ increases significantly on the interval 50 < Re < 300, before incurring a significant decrease for 800 < Re < 5000, similar to tends observed for C_L'. However, C_D' incurs a

relatively minor (≈50%) decrease for $800 < \mathrm{Re} < 5000$ in magnitude whereas C_L' [Fig. 7(a)] incurs nearly a 90% decrease. This is due to the rise of energy at low frequencies which now dominates C_D' in this regime (Fig. 8). For $\mathrm{Re} > 5000$, inspection of the previously published drag traces [9,84] indicates that significant fluctuations occur once again at $2f_S$, comparable to fluctuations at lower frequencies. The high degree of scatter in Fig. 7(c) is hence attributed primarily to the low frequency component variations in the drag force [93], which require large sampling intervals for accurate measurement and may be sensitive to free-stream turbulence parameters [86,94].

B. Vortex tracking and statistics

As Re is increased and the cylinder wake undergoes laminar-to-turbulent transition (Fig. 4), the secondary vortex dynamics show distinct topological changes which occur in conjunction with large changes in fluctuating loads (Fig. 7). This motivates investigation of the integral effects secondary vortex development has on the primary shedding instability, to understand its influence on the structural loading. Holistically, the sectional fluctuating loads can decrease for three reasons: (i) the formation length (l_f) contracts, weakening the surface pressure fluctuations induced by the primary vortices, (ii) symmetric modes are excited near the surface, increasing the correlation of fluctuating surface pressures on opposing sides of the cylinder, or (iii) the circulation of the primary vortices decreases, weakening their induced fluctuations. Indeed, the large decrease in C_L' and C_D' [Figs. 7(a) and 7(c)] for $800 < \mathrm{Re} < 5000$ has been associated with both an increase in l_f and an increase in correlation of the surface pressures acting on the opposing shoulders of the cylinder [88]. However, it has been conjectured that the secondary vortices can act to decrease the circulation of the spanwise vortices [29,34,35], whereas models of formation region dynamics typically assume constant circulation with Re [32]. With access to the validated three-dimensional DNS data (Figs. 6 and 7), the effect of secondary vortex circulation can be determined from careful tracking and quantification of vortex statistics in the wake.

The secondary vortex statistics are calculated using the iterative code with a starting y-z plane at $x/D = 2.5$. To filter out erroneous identification of spanwise rollers as secondary structures, vortices oriented within a 20° solid angle ($\gamma > 20°$) of the z axis were rejected. Decreasing this rejection angle causes a significant increase of the mean circulation and vortex diameter statistics, indicating it is a good threshold for rejecting erroneously detected spanwise vortices, which characteristically have higher vortex diameter and circulation. Figure 9(a) shows a sample result of the vortex detection code for $\mathrm{Re} = 300$. The figure verifies that the code converges correctly on all the streamwise vortex cores passing through the y-z plane at $x/D = 2.5$. Each detected secondary vortex has an associated mean orientation [$\bar{\boldsymbol{\omega}}^j$, black arrows, Fig. 9(a)] along with an enclosed vorticity component in the direction of mean orientation [$\boldsymbol{\omega} \cdot \hat{\mathbf{n}}$, yellow and purple contours, Fig. 9(a)], while the closed contour encompassing $Q < 0.01$ [white isosurfaces, Fig. 9(a)] is used to define each vortex area Ω^j. The vortex area is seen to encapsulate the majority of the vorticity of the secondary vortices with minimal discrepancies in shape and location compared to the vorticity contours. Such agreement is expected for vortex detection based on Q-criterion in the wake, since viscous effects and unsteady irrotational straining [95] are minimal outside the formation region where secondary vortices primarily advect in the wake.

Figures 9(b)–9(e) show the joint probability distributions of vortex inclination [$\beta = \tan^{-1}(\bar{\omega}_y/\bar{\omega}_x)$] with respect to the streamwise axis and the transverse centroid position ($\bar{y}$) from the wake centreline for each Re. In each case, there are two concentrated bands spanning $-45° < \beta < 0°$ and $0° < \beta < 45°$ for $\mathrm{Re} = 220$ [Fig. 9(b)], and expanding to $-70° < \beta < 30°$ and $-30° < \beta < 70°$ for $\mathrm{Re} = 1575$ [Fig. 9(e)], indicative of the increase in disorder in $B+$ wake transition for $\mathrm{Re} \gtrsim 800$. The dependence of β on $\bar{y}$ is due to the curvature of the vortex structures in the wake, which wrap around the main spanwise rollers along the principal strain directions [13,20]. This renders the measurement of vortex angle in the wake dependent on sampling position. For mode A and mode B vortex formation [Figs. 9(b) and 9(c)], β is distributed along a narrow band, indicative of the more organized structure of the wake, which can also be seen in velocity phase space traces

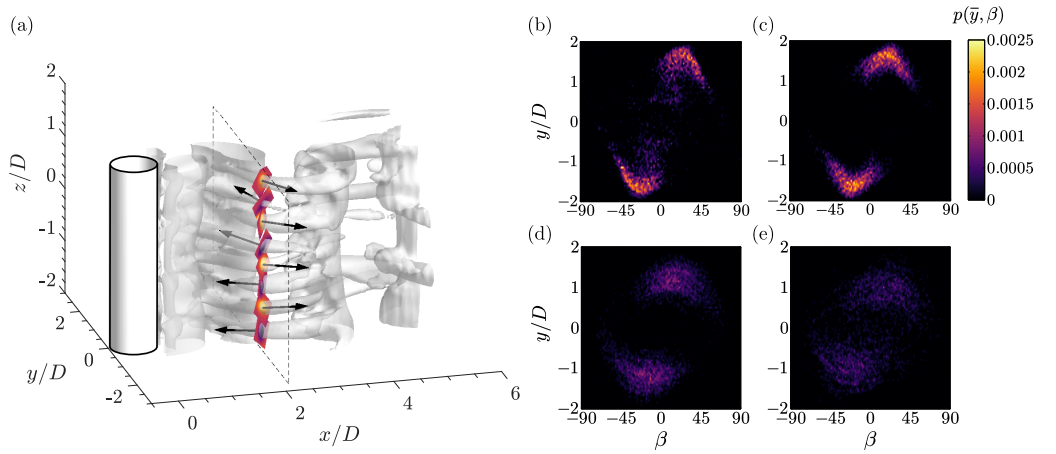

FIG. 9. (a) Visualization of secondary vortex identification results for Re = 300, arrows denote orientation and relative magnitude of mean vorticity in each vortex core. The orientation of the secondary vortices with respect to the x axis (β) is tracked as the cores advect past a sample y-z plane at $x/D = 2.5$ and its joint probability distribution with transverse centroid position ($\bar{y}$) is plotted for (b) Re = 220, (c) Re = 300, (d) Re = 800, and (e) Re = 1575.

in Karniadakis and Triantafyllou [19], which show a low-dimensional attractor governing the flow field dynamics for this Re range. For Re = 220 [Fig. 9(b)], the mode A vortex loops are found in the probability distribution [$p(\bar{y}, \beta)$] as a wider band distributed closer to $\beta = 0$ and closer to the wake centreline ($y = 0$) than the mode B structures. Since the mode B structures have smaller λ_z (Fig. 6), they occur more frequently than the mode A structures, hence the probability density function is weighted more strongly toward showing mode B structures, even though the wake state is mode A^* for the majority of the sample. For Re = 800 and Re = 1575, a significant broadening of the probability distributions is observed as secondary vortices occupy positions closer to the wake centreline and are strained and tilted more significantly, marking the transition of the wake past mode B.

The changes in the complexity of the vortex dynamics in the wake with Re may also be elucidated through an sPOD analysis. Figure 10 shows the relative energy spectra across the sPOD modes for each Re. The amount of relative energy in the first two sPOD modes decreases with Re from 0.96 for Re = 100 to 0.42 for Re = 1575. The exception to the trend is Re = 220, which has less energy in the first two modes compared to Re = 300. This is due to the vortex dislocations present in the mode A^* state (Fig. 4), causing a significant amount of the energy to spread to the third and fourth modes (0.15), which are associated with angular deformation of the primary rollers. Indeed, the combined energy of the first four modes remains higher for Re = 220 than 300 (Fig. 10). Besides the decrease in relative energy content in the most energetic modes for increasing Re, topologically different behavior of the tails of the spectra can also be discerned from Fig. 10. Specifically, the entirely two-dimensional instability present for Re = 100 leads to a rapidly decaying energy spectrum as harmonic pairs of the primary instability cascade. For the initial three-dimensional instabilities, A^* and B, the decay of energy in the higher modes is less rapid, and though they have different distributions of relative energy in the first few modes, the tails collapse onto similar profiles. Presumably, mutual interactions of the A^* and B instabilities with the 2D instability and its harmonics causes the spread of energy to the higher modes. For Re = 800 and 1575, a clear distinction can be made from the other Re cases, with the exponential decay of the energy content delayed until approximately the 400–500th mode. The relatively high amount of energy being spread out over the first few hundred modes is associated with a change in the topology to a more complex attractor for the dynamics [23], indicative of a more chaotic wake dynamics stemming from transition to the $B+$ state. Thus, this signature in the sPOD modal energy spectrum can serve to identify the onset of the B+ mode.

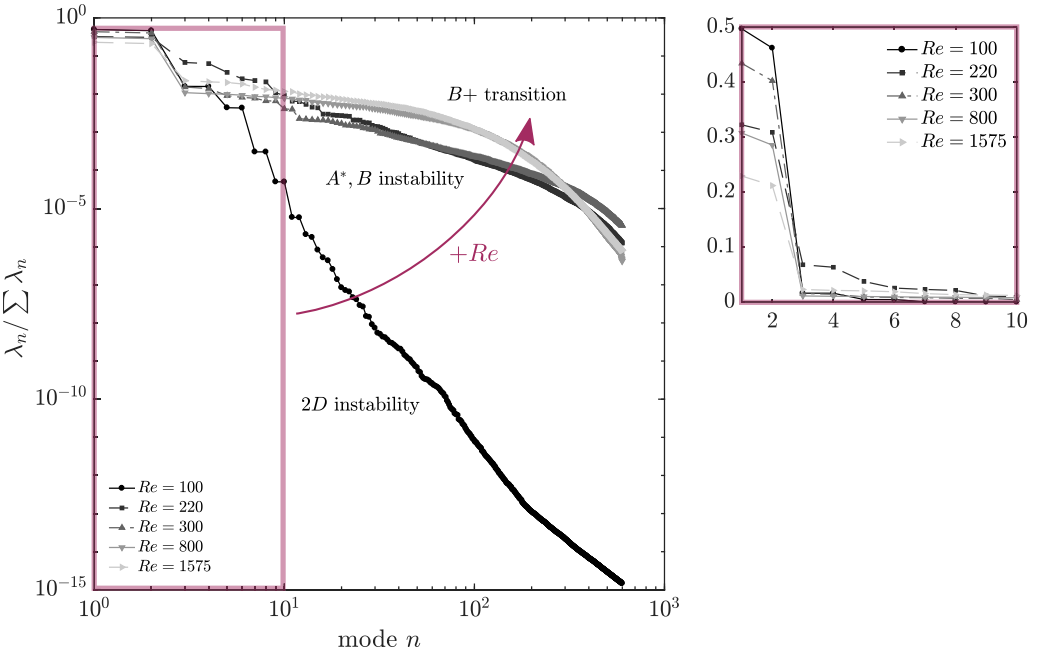

FIG. 10. sPOD modal energy distribution.

Figure 11 compares three-dimensional isosurfaces of the streamwise component of the first five sPOD modes for Re = 1575. The results demonstrate that the first two modes [Figs. 11(a) and 11(b)] form a pair representing the primary two-dimensional global instability of the flow for every Re, with corresponding temporal coefficients fluctuating at f_S. The third mode [Fig. 11(c)] is an unpaired mode, symmetric about the wake centreline, whose temporal coefficient is dominated by low frequency activity and is the well-known shift-mode modulating cylinder wake activity [42,43]. Notably, in three dimensions, the shift mode has substantial spanwise variation and reverses sign after some spanwise distance. This indicates that the wake modulation effects are correlated only along a finite spanwise length, and the damping and enhancement of the primary shedding instability

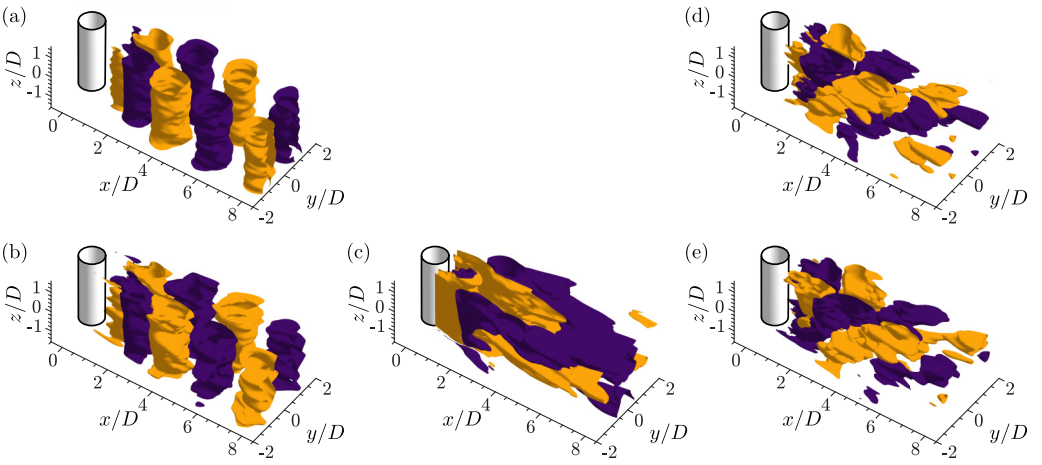

FIG. 11. Isosurfaces of streamwise velocity for the first five (a)–(e) normalized POD mods for Re = 1575 (yellow, $u/U_o = 0.6 \times 10^{-3}$; purple, $u/U_o = -0.6 \times 10^{-3}$).

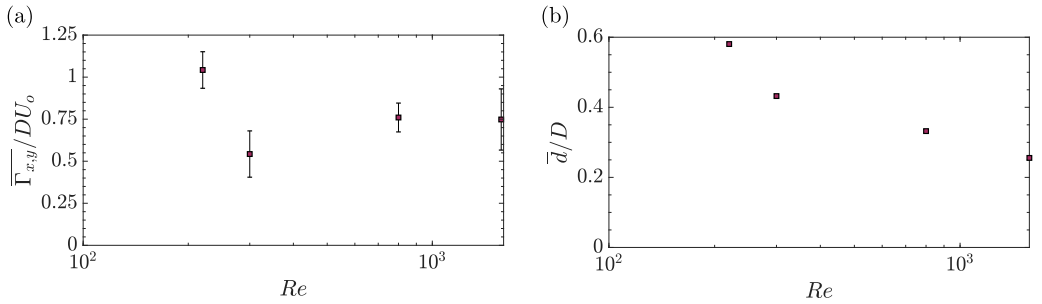

FIG. 12. Properties of secondary vortices (a) mean circulation ($\overline{\Gamma_{x,y}}$) and (b) mean vortex diameter ($\overline{d}$) at $x/D = 2.5$.

varies continuously along the span at any given time. The fourth and fifth modes [Figs. 11(d) and 11(e)] form a pair representing oblique shedding of primary vortices, similar to the first and second modes capturing primary shedding. For Re = 220–800, the oblique mode pair is more energetic than the shift mode and forms the third and fourth modes instead.

Figures 12(a) and 12(b) show the variation of the mean circulation and diameter of the secondary vortices with Re. The circulation is measured by the area integral of plane-normal vorticity over Ω^j [Eq. (4)] and the vortex diameter is defined as the diameter of the circle whose area matches the area of Ω^j [Eq. (3)]. The mean circulation of the secondary vortices is at a maximum of $\overline{\Gamma}_{x,y}/U_oD = 1.04$ for Re = 220 [Fig. 12(a)], at a minimum of $\overline{\Gamma}_{x,y}/U_oD = 0.53$ for Re = 220, and remains approximately constant at $\overline{\Gamma}_{x,y}/U_oD = 0.75$–$0.76$ for Re $\geqslant$ 800. The mean vortex diameter is at a maximum of $\overline{d}/D = 0.59$ for Re = 220 and decreases with increased Re [Fig. 12(b)]. The decrease in vortex diameter with increasing or constant circulation for Re $\geqslant$ 300 implies an increase in straining of the secondary vortices with increasing Re, associated with the generation of turbulence.

Measurements of the strength of the streamwise vortices ($\Gamma_{x,y}$) facilitates a discussion about the influence of the reorientation of spanwise vorticity in the wake on the strengths of the primary rollers. The goal is to determine whether the secondary instability growth can be directly linked to weakening of the spanwise vortices and held partly responsible for the observed changes in fluctuating loads (Fig. 7) with Re and for modified cylinder geometries [34,35]. A balance of the spanwise vorticity transport is constructed [Eq. (13)] such that the production of spanwise vorticity, $\tilde{K}_S$ [96] at the cylinder wall in the upper half plane is balanced by the vorticity advection by the primary vortices, $K_z = \overline{\Gamma}_z f_S$, the reorientation of vorticity into streamwise or transverse oriented vortices, $K_{x,y}$, and the vorticity annihilation with opposing vorticity bearing fluid from the lower half plane, K_a. For quantitative analysis, $\tilde{K}_S$ is calculated using the mean advected vorticity from each separated shear layer $\tilde{K}_S = \int_0^{L_z}\int_0^{\infty} \overline{u(D/2,y,z)\omega_z(D/2,y,z)}dydz$, K_z is calculated by a measurement of the phase-averaged strength of the wake vortices and the shedding frequency $K_z = \overline{\Gamma_z} f_S$, and $K_{x,y}$ is estimated assuming the secondary vortices form in opposing pairs in the wake, leading to a reduction in the advected spanwise vorticity of $K_{x,y} = \overline{\Gamma_{x,y}[1-\cos(\gamma)]} f_S$, where γ is the solid angle of the orientation of each secondary vortex with the spanwise axis:

$$\tilde{K}_S = K_z + K_{x,y} + K_a. \tag{13}$$

The vorticity balance terms K_z, $K_{x,y}$, and K_a vary with increasing streamwise distance, generally leading to increasing K_a and decreasing K_z and $K_{x,y}$. However, the main variations occur due to the highly unsteady mixing during vortex formation, which is the primary region of interest since its proximity to the surface implies the strongest effects on structural loading characteristics (Fig. 7). Hence, measurements of the advective quantities in Eq. (13) are evaluated at $x/D = 2.5$,

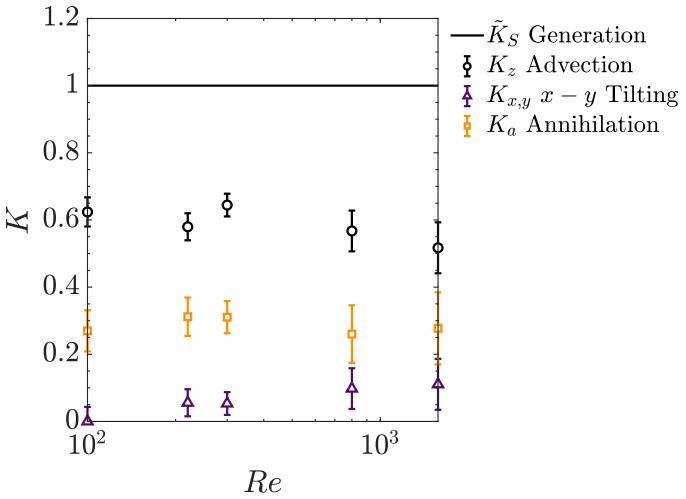

FIG. 13. Transport of spanwise vorticity after generation at the cylinder wall ($\tilde{K}_S$), advection in the wake (K_z), reorientation into transverse or streamwise vorticity in the wake ($K_{x,y}$), and cross-annihilation of vorticity (K_a).

immediately following vortex formation. The annihilation term (K_a) is determined from Eq. (13) based on the estimated values of $\tilde{K}_S$, K_z, and $K_{x,y}$.

Figure 13 plots the respective terms in Eq. (13) for each Re. The results indicate that the proportion of spanwise vorticity ($K_{x,y}$) reoriented in the transverse and streamwise directions in the wake increases with Re (Fig. 13). However, while a general decreasing trend can be discerned in the proportion of spanwise vorticity advected by the primary vortices (K_z) with increasing Re, the data at Re $= 300$ deviates from this trend. This is likely attributed to the fact that the mode B vortices, which dominate the secondary vortex developments for Re $= 300$, form due to a hyperbolic instability in the vorticity braids connecting the primary vortices [12], whose contribution is not explicitly accounted for in Eq. (13). In contrast, the elliptic instability in mode A^* at Re $= 220$ directly involves the primary rollers causing reorientation of vorticity. Similarly, for Re $= 800$ and Re $= 1575$, the pinching formation mechanism for the hairpin vortices in $B+$ transition identified in Figs. 4(d) and 5 causes explicit reorientation. As a result, the vorticity advected in the primary rollers (K_z) decreases after $B+$ transition for Re > 300, while the proportion annihilated across the wake (K_a) showing no discernible trend with Re. The decrease in the relative strength of the vortices with increased Re due to the vorticity reorienting mechanism for Re > 300 is therefore concluded to have a subsidiary role in the large decrease in C'_L and C'_D for Re $\geqslant 300$ [Figs. 7(a) and 7(c)], as the change in relative strength of the primary vortices that can be attributed to spanwise reorientation is approximately 20%, compared to the approximately 90% decrease in the fluctuating loads. However, the precise quantitative effect is contingent on the uncertainty in circulation measurements indicated in Fig. 13. The significance of a relative decrease in the strength of the primary vortices of 20% can be inferred from inviscid models of the von Kármán wake [97], which predict lift fluctuations scale linearly with dimensionless spanwise vortex circulation ($C_{L,\max} = u_{\text{adv}}\Gamma_z/U_o^2 D$), which is further compounded by the advective velocity (u_{adv}) being proportional to Γ_z.

IV. CONCLUSIONS

Direct numerical simulations of a circular cylinder in cross flow are performed for Re $= 100$, 220, 300, 800, 1575. The results indicate a route of transition in the cylinder wake of $2D \rightarrow A^* \rightarrow B \rightarrow B+$, where $B+$ denotes a wake containing mode B instabilities straddled with hairpin vortices. The $B+$ regime is characterized by a significant increase in vortex deformation and irregularity in

the wake along with a plethora of hairpin formations. The DNS simulations were validated against previous experimental and numerical measurements of C_L', $\overline{C_D}$, and C_D'. In particular, a compilation of sources is used to construct a representative plot of C_D' over a wide range of Re that revealed the significant data scatter within and between studies. An analysis of the compiled drag force fluctuation data showed a relation between high data scatter and regimes where low frequency fluctuations dominate for transitional and turbulent shedding regimes.

To facilitate the quantitative analysis of the vortex dynamics in the $B+$ transitional regime, a three-dimensional vortex tracking algorithm was developed. The algorithm seeks to detect the orientation, circulation, area, and centroid position of every vortex in a given sample plane. The three-dimensional algorithm has the benefit of avoiding smearing of the structures onto a measurement plane misaligned with each vortex orientation. The results indicate mean vortex diameter contracts with Re, indicative of the higher vorticity stretching associated with increased turbulent generation in the wake, and mean streamwise vortex circulation remains relatively constant, besides the stronger mode A vortices for $\mathrm{Re} = 220$. Broadening of the joint probability distributions of the streamwise vortex inclination angle with the transverse centroid position in the wake are indicative of the transition from relatively simple limit cycles governing the dynamics for $\mathrm{Re} = 220$ and $\mathrm{Re} = 300$, where vortex formation is predictable, to a more complex turbulent state for $\mathrm{Re} \geqslant 800$, due to a high degree of deformation and chaotic vortex formations in the wake, marking the $B+$ wake transition. An sPOD analysis is conducted to provide insight into the modal behavior of the wake through transition. The results indicate that the relative energy content contained in the first two modes decreases with Re significantly, spreading out to higher-order modes. In addition, the modal energy spectrum serves as a good marker for $B \rightarrow B+$ transition, when the tail of the spectrum attains significant energy due to the dynamics switching to higher dimensional attractors.

Quantitative analysis of the distribution of vortex strength and vorticity transport at the cylinder surface and in the wake reveals a minor decrease in the average spanwise vortex strength with increasing Re, attributed to vorticity reorientation caused by the mechanism of hairpin vortex formation in the $B+$ regime for $\mathrm{Re} \geqslant 800$. The annihilation of vorticity across the wake centerline is shown to stay relatively constant with Re, consistent with earlier studies attributing it to an inviscid mechanism. The identified decrease of about 20% in the advection of spanwise vorticity in the primary vortices caused by spanwise vortex reorientation is therefore ascribed as a subsidiary cause for the major reduction ($\approx$90%) of fluctuating loads for $\mathrm{Re} \geqslant 800$.

ACKNOWLEDGMENT

The authors gratefully acknowledge the contribution of the Natural Science and Engineering Research Council (NSERC) to the funding of this research.

[1] M. Provansal, C. Mathis, and L. Boyer, Benard-von Karman instability: Transient and forced regimes, J. Fluid Mech. **182**, 1 (1987).
[2] P. W. Bearman, Circular cylinder wakes and vortex-induced vibrations, J. Fluids Struct. **27**, 648 (2011).
[3] R. D. Blevins, Flow-induced vibration, J. Appl. Mech. **44**, 802 (1986).
[4] M. M. Zdravkovich, Review and classification of various aerodynamics and hydrodynamics means for suppressing vortex shedding, J. Wind Eng. Industr. Aerodynam. **7**, 145 (1981).
[5] R. D. Blevins, Review of sound induced by vortex shedding from cylinders, J. Sound Vib. **92**, 455 (1984).
[6] J. McClure, C. Morton, and S. Yarusevych, Flow development and structural loading on dual step cylinders in laminar shedding regime, Phys. Fluids **27**, 063602 (2015).
[7] C. Morton and S. Yarusevych, On vortex shedding from low aspect ratio dual step cylinders, J. Fluids Struct. **44**, 251 (2014).

[8] J. H. M. Fransson, P. Konieczny, and P. H. Alfredsson, Flow around a porous cylinder subject to continuous suction or blowing, J. Fluids Struct. **19**, 1031 (2004).
[9] T. N. Jukes and K. S. Choi, Flow control around a circular cylinder using pulsed dielectric barrier discharge surface plasma, Phys. Fluids **21**, 084103 (2009).
[10] H. Choi, W. P. Jeon, and J. Kim, Control of flow over a bluff body, Annu. Rev. Fluid Mech. **40**, 113 (2008).
[11] D. Barkley and R. D. Henderson, Three-dimensional Floquet stability analysis of the wake of a circular cylinder, J. Fluid Mech. **322**, 215 (1996).
[12] C. H. K. Williamson, Three-dimensional wake transition, J. Fluid Mech. **328**, 345 (1996).
[13] M. C. Thompson, T. Leweke, and C. H. K. Willaimson, The physical mechanism of transition in bluff body wakes, J. Fluids Struct. **15**, 607 (2001).
[14] H. Jiang, L. Cheng, F. Tong, S. Draper, and H. An, Stable state of Mode A for flow past a circular cylinder, Phys. Fluids **28**, 104103 (2016).
[15] C. H. K. Williamson, The natural and forced formation of spotlike "vortex dislocations" in the transition of a wake, J. Fluid Mech. **243**, 393 (1992).
[16] L. Qu, C. Norberg, L. Davidson, S. H. Peng, and F. Wang, Quantitative numerical analysis of flow past a circular cylinder at Reynolds number between 50 and 200, J. Fluids Struct. **39**, 347 (2013).
[17] F. Scarano and C. Poelma, Three-dimensional vorticity patterns of cylinder wakes, Exp. Fluids **47**, 69 (2009).
[18] H. Jiang, L. Cheng, S. Draper, H. An, and F. Tong, Three-dimensional direct numerical simulation of wake transitions of a circular cylinder, J. Fluid Mech. **801**, 353 (2016).
[19] G. E. Karniadakis and G. S. Triantafyllou, Three-dimensional dynamics and transition to turbulence in the wake of bluff objects, J. Fluid Mech. **238**, 1 (1992).
[20] C. H. K. Williamson, Vortex dynamics in the cylinder wake, Annu. Rev. Fluid Mech. **28**, 477 (1996).
[21] R. Mittal and S. Balachandar, Generation of Streamwise Vortical Structures in Bluff Body Wakes, Phys. Rev. Lett. **75**, 1300 (1995).
[22] A. G. Tomboulides, G. S. Triantafyllou, and G. E. Karniadakis, A new mechanism of period doubling in free shear flows, Phys. Fluids **4**, 1329 (1992).
[23] R. Henderson, Nonlinear dynamics and pattern formation in turbulent wake transition, J. Fluid Mech. **352**, 65 (1997).
[24] M. S. Bloor, The transition to turbulence in the wake of a circular cylinder, J. Fluid Mech. **19**, 290 (1964).
[25] A. Prasad and C. Williamson, Three-dimensional effects in turbulent bluff-body wakes, J. Fluid Mech. **343**, 235 (1997).
[26] B. Muchmore and A. Ahmed, On streamwise vortices in turbulent wake of cylinders, Phys. Fluids A **5**, 387 (1993).
[27] T. Wei and C. Smith, Secondary vortices in the wake of circular cylinders, J. Fluid Mech. **169**, 513 (1986).
[28] J. Wu, J. Sheridan, M. Welsh, K. Hourigan, and M. Thompson, Longitudinal vortex structures in a cylinder wake, Phys. Fluids **6**, 2883 (1994).
[29] J. Huang, Y. Zhou, and T. Zhou, Three-dimensional wake structure measurement using a modified PIV technique, Exp. Fluids **40**, 884 (2006).
[30] J. Wu, J. Sheridan, J. Soria, and M. Welch, An experimental investigation of streamwise vortices in the wake of a bluff body, J. Fluids Struct. **8**, 621 (1994).
[31] M. Brede, H. Eckelmann, and D. Rockwell, On secondary vortices in the cylinder wake, Phys. Fluids **8**, 2117 (1996).
[32] J. H. Gerrard, The mechanics of the vortex formation region of vortices behind bluff bodies, J. Fluid Mech. **25**, 401 (1966).
[33] C. Chyu and D. Rockwell, Evolution of patterns of streamwise vorticity in the turbulent near wake of a circular cylinder, J. Fluid Mech. **320**, 117 (1996).
[34] J. McClure and S. Yarusevych, Vortex shedding and structural loading characteristics of finned cylinders, J. Fluids Struct. **65**, 138 (2016).
[35] I. Yildirim, C. Rindt, and A. van Steenhoven, Energy contents and vortex dynamics in Mode-C transition of wired-cylinder wake, Phys. Fluids **25**, 054103 (2013).

[36] J. L. Lumley, The structure of inhomogeneous turbulent flows, in *Atmospheric Turbulence and Radio Wave Propagation* (Nauka, Moscow, 1967).
[37] A. E. Deane, I. G. Kevrekidis, G. E. Karniadakis, and S. A. Orszag, Low-dimensional models for complex geometry flows: Application to grooved channels and circular cylinders, Phys. Fluids **3**, 2337 (1991).
[38] X. Ma, G. S. Karamanos, and G. E. Karniadakis, Dynamics and low-dimensionality of a turbulent near wake, J. Fluid Mech. **410**, 29 (2000).
[39] B. W. Oudheusden, F. Scarano, N. P. Hinsberg, and D. W. Watt, Phase resolved characterization of vortex shedding in the near wake of a square-section cylinder at incidence, Exp. Fluids **39**, 86 (2005).
[40] R. Perrin, M. Braza, E. Cid, S. Cazin, A. Barthet, A. Sevrain, C. Mockett, and F. Thiele, Obtaining phase averaged turbulence properties in the near wake of a circular cylinder at high Reynolds number using POD, Exp. Fluids **43**, 341 (2007).
[41] R. Perrin, C. Mockett, M. Braza, and E. Cid, Joint numerical and experimental investigation of the flow around a circular cylinder at high Reynolds number in particle image velocimetry, Top. Appl. Phys. **112**, 223 (2007).
[42] B. R. Noack, K. Afanasiev, M. Morzynski, G. Tadmor, and F. Thiele, A hierarchy of low-dimensional models for the transient and post-transient cylinder wake, J. Fluid Mech. **497**, 335 (2003).
[43] J. Bourgeois, B. Noack, and R. Martinuzzi, Generalized phase average with applications to sensor-based flow estimation of the wall-mounted square cylinder wake, Phys. Fluids **736**, 316 (2013).
[44] T. K. Sengupta, S. I. Haider, M. K. Parvatha, and G. Pallavi, Enstrophy-based proper orthogonal decomposition for reduced-order modeling of flow past a cylinder, Phys. Rev. E **91**, 043303 (2015).
[45] S. Scharnowski, V. Statnikov, M. Meinke, W. Schröder, and C. J. Kähler, Combined experimental and numerical investigation of a transonic space launcher wake, EUCASS Proc. Ser. Adv. AeroSpace Sci. Progr. Flight Phys. **7**, 311 (2015).
[46] C. Morton and S. Yarusevych, Vortex shedding in the wake of a step cylinder, Phys. Fluids **22**, 083602 (2010).
[47] O. Inoue and A. Sakuragi, Vortex shedding from a circular cylinder of finite length at low Reynolds numbers, Phys. Fluids **20**, 033601 (2008).
[48] P. Moin and K. Mahesh, Direct numerical simulation: A tool in turbulence research, Annu. Rev. Fluid Mech. **30**, 539 (1998).
[49] J. G. Wissink and W. Rodi, Numerical study of the near wake of a circular cylinder, Int. J. Heat Fluid Flow **29**, 1060 (2008).
[50] M. Zhao and L. Cheng, Vortex-induced vibration of a circular cylinder of finite length, Phys. Fluids **26**, 015111 (2014).
[51] H. Jiang, L. Cheng, and H. An, On numerical aspects of simulating flow past a circular cylinder, Int. J. Numer. Methods Fluids **85**, 113 (2017).
[52] S. C. Kacker, B. Pennington, and R. S. Hill, Fluctuating lift coefficient for a circular cylinder in cross flow, J. Mech. Eng. Sci. **16**, 215 (1974).
[53] M. Rockwood, Y. Huang, and M. Green, Tracking coherent structures in massively-separated and turbulent flows, Phys. Rev Fluids **3**, 014702 (2018).
[54] L. Sirovich, Turbulence and the dynamics of coherent structures, parts I–III, Q. Appl. Math. **45**, 561 (1987).
[55] J. C. R. Hunt, A. A. Wray, and P. Moin, Eddies, streams, and convergence zones in turbulent flows, in *Proceedings of the Summer Program*, N89-24555 (Center for Turbulence Research, Stanford, CA, 1988).
[56] C. H. K. Williamson, Oblique and parallel modes of vortex shedding in the wake of a circular cylinder at low Reynolds numbers, J. Fluid Mech. **206**, 579 (1989).
[57] S. Rajagopalan and R. A. Antonia, Flow around a circular cylinder—Structure of the near wake shear layer, Exp. Fluids **38**, 393 (2005).
[58] A. Roshko, Perspectives of bluff body aerodynamics, J. Wind Eng. Industr. Aerodynam. **49**, 79 (1993).
[59] M. F. Unal and D. Rockwell, The role of shear layer stability in vortex shedding from cylinders, Phys. Fluids **27**, 2598 (1984).
[60] O. Posdziech and R. Grundmann, Numerical simulation of the flow around an infinitely long circular cylinder in the transition regime, Theor. Comput. Fluid Dyn. **15**, 121 (2001).

[61] H. Q. Zhang, U. Fey, B. R. Noack, M. König, and H. Eckelmann, On the transition of the cylinder wake, Phys. Fluids **7**, 779 (1995).
[62] H. Mansy, P. Yang, and D. Williams, Quantitative measurements of the three-dimensional structures in the wake of a circular cylinder, J. Fluid Mech. **270**, 277 (1994).
[63] See Supplemental Material at http://link.aps.org/supplemental/10.1103/PhysRevFluids.4.124702 for visualization of wake vortex shedding.
[64] C. Wieselsberger, New data on the law of hydro and aerodynamic resistance, Phys. Z. **22**, 321 (1921).
[65] O. Marzouk, A. H. Nayfeh, I. Akhtar, and H. N. Arafat, Modeling steady-state and transient forces on a cylinder, J. Vibrat. Control **13**, 1065 (2007).
[66] C. Liu, X. Zheng, and C. H. Sung, Preconditioned multigrid methods for unsteady incompressible flows, J. Comput. Phys. **139**, 35 (1998).
[67] R. D. Henderson, Details of the drag curve near the onset of vortex shedding, Phys. Fluids **7**, 2102 (1995).
[68] C. Evangelinos and G. Karniadakis, Dynamics and flow structures in the turbulent wake of rigid and flexible cylinders subject to vortex-induced vibrations, J. Fluid Mech. **400**, 91 (1999).
[69] P. Batcho and G. Karniadakis, Chaotic transport in two- and three-dimensional flow past a cylinder, Phys. Fluids **3**, 1051 (1991).
[70] V. Kalro and T. Tezduyar, Parallel 3D computation of unsteady flows around circular cylinders, Parallel Computing **23**, 1235 (1997).
[71] X. Lu, C. Dalton, and J. Zhang, Application of large eddy simulation to flow past a circular cylinder, J. Offshore Mech. Arctic Eng. **119**, 221 (1997).
[72] Rajat Mittal and S. Balachandar, Effect of three dimensionality on the lift and drag of nominally two dimensional cylinders, Phys. Fluids **7**, 1841 (1995).
[73] J. Zhang and C. Dalton, A three-dimensional simulation of a steady approach flow past a circular cylinder at low Reynolds number, Int. J. Numer. Methods Fluids **26**, 1003 (1998).
[74] J. H. Gerrard, An experimental investigation of the oscillating lift and drag of a circular cylinder shedding turbulent vortices, J. Fluid Mech. **11**, 244 (1961).
[75] D. M. McGregor, An experimental investigation of the oscillating pressures on a circular cylinder in a fluid stream, Ph.D. thesis, Department of Aeronautical Engineering and Aerophysics, University of Toronto, 1957.
[76] G. S. West and C. J. Apelt, Measurements of fluctuating pressures and forces on a circular cylinder in the Reynolds number range 10^4 to 2.5×10^5, J. Fluids Struct. **7**, 227 (1993).
[77] P. Sonneville, Etude de la structure tridimensionelle des écoulements autour d'un cylindre circulaire, Bulletin de la Direction des Etudes et Recherches, Serie A, No. 3 (1976).
[78] J. P. Batham, Pressure distributions on circular cylinders at critical Reynolds numbers, J. Fluid Mech. **57**, 209 (1973).
[79] M. M. Alam, H. Sakamoto, and M. Moriya, Reduction of fluid forces acting on a single circular cylinder and two circular cylinders by using tripping rods, J. Fluids Struct. **18**, 347 (2003).
[80] M. M. Alam, M. Moriya, K. Takai, and H. Sakamoto, Fluctuating fluid forces acting on two circular cylinders in a tandem arrangement, J. Wind Eng. Industr. Aerodynam. **91**, 139 (2003).
[81] M. M. Alam, Y. Zhou, J. M. Zhao, O. Flamand, and O. Boujard, Classification of the tripped cylinder wake and bi-stable phenomenon, Int. J. Heat Fluid Flow **31**, 545 (2010).
[82] S. Szepressy and P. W. Bearman, Aspect ratio and end plate effects on vortex shedding from a circular cylinder, J. Fluid Mech. **234**, 191 (1992).
[83] F. Bouak and J. Lemay, Passive control of the aerodynamic forces acting on a circular cylinder, Exp. Therm. Fluid Sci. **16**, 112 (1998).
[84] Y. C. Fung, Fluctuating lift and drag acting on a cylinder in a flow at supercritical Reynolds numbers, J. Aerosp. Sci. **27**, 801 (1960).
[85] K. Lam, J. Y. Li, and R. M. C. So, Force coefficient and Strouhal numbers of four cylinders in cross flow, J. Fluids Struct. **18**, 305 (2003).
[86] J. McClure and S. Yarusevych, Surface and wake pressure fluctuations of a cylinder in transitional flow regime, in *Proceedings of the 18th International Symposium on the Application of Laser and Imaging Techniques to Fluid Mechanics* (Lisbon, Portugal, 2016).

[87] H. Tennekes and J. L. Lumley, *A First Course in Turbulence* (MIT Press, Cambridge, MA, 1972).
[88] C. Norberg, Fluctuating lift on a circular cylinder: Review and new measurements, J. Fluids Struct. **17**, 57 (2003).
[89] S. Dong, G. Karniadakis, A Ekmekci, and D. Rockwell, A combined direct numerical simulation-particle image velocimetry study of the turbulent near wake, J. Fluid Mech. **569**, 185 (2006).
[90] N. Jauvtis and C. H. K. Williamson, The effect of two degrees of freedom on vortex-induced vibration at low mass and damping, J. Fluid Mech. **509**, 23 (2004).
[91] J. M. Dahl, F. S. Hover, and M. S. Triantafyllou, Two-degree-of-freedom vortex-induced vibrations using a force assisted apparatus, J. Fluids Struct. **22**, 807 (2006).
[92] A. Sanchis, G. Saelevik, and J. Grue, Two-degree-of-freedom vortex-induced vibrations of a spring-mounted rigid cylinder with low mass ratio, J. Fluids Struct. **24**, 907 (2008).
[93] O. Lehmkuhl, I. Rodríguez, R. Borrell, and A. Oliva, Low-frequency unsteadiness in the vortex formation region of a circular cylinder, Phys. Fluids **25**, 085109 (2013).
[94] A. K. Norman and B. J. McKeon, Unsteady force measurements in sphere flow from subcritical to supercritical Reynolds numbers, Exp. Fluids **51**, 1439 (2011).
[95] G. Haller, An objective definition of a vortex, J. Fluid Mech. **525**, 1 (2005).
[96] E. Berger and R. Wille, Periodic flow phenomena, Annu. Rev. Fluid Mech. **4**, 313 (1972).
[97] Y. N. Chen, Fluctuating lift forces of the Karman vortex streets on single circular cylinders and in tube bundles. Part 2. Lift forces of single cylinders, J. Eng. Ind. **94**, 613 (1971).